Electronic Supplementary Information

Interconnected Metal Oxide CNT Fibre Hybrid Networks for Current Collector-Free Asymmetric Capacitive Deionization

Cleis Santos,[a] Julio J. Lado,* [b] Enrique García-Quismondo, [b] Inés Vázquez Rodríguez, Daniel Hospital Benito, Jesús Palma, Marc A. Anderson [b, c] and Juan J. Vilatela,* [a]

a. *IMDEA Materials Institute. Tecnogetafe. Eric Kandel, 2, 28906, Getafe, Madrid, Spain*
** Email: juanjose.vilatela@imdea.org*
b. *IMDEA Energy Institute. Parque Tecnológico de Móstoles. Avda. Ramón de la Sagra, 3, 28933, Móstoles, Madrid, Spain*
** Email: julio.lado@imdea.org*
c. *Department of Civil and ENVIRONMENTAL Engineering, University of Wisconsin-Madison, 53706, WI, USA*

Capacitive deionization (CDI) technology. CDI, is an emerging desalination technology able to reduce the salt concentration of a water stream by establishing a potential difference between two porous carbon electrodes (capacitor charge step, **Figure S1**a). Once the electrodes are saturated due to the salt adsorption in the electric double-layer (EDL), the ion desorption is forced by short-circuiting the cell (capacitor discharge step, Figure S1b). In this fashion, CDI technology is able to deliver water while storing energy in the EDL. The stored energy could be subsequently retrieved in the electrode discharge step using the same working principle as a capacitor (Figure S1b).

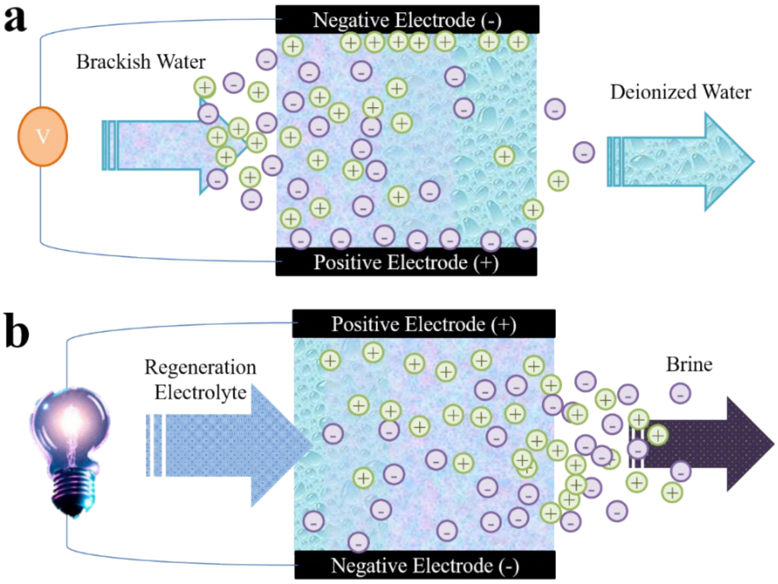

Figure S1. CDI process scheme: **a)** Ion Removal-Charging stage. **b)** Ion Release-Discharging step.

CDI Experimental Set-Up. A filter-press CDI laboratory cell provided by Proingesa (Spain) was assembled placing the MOx/CNTf coated with γ-Al_2O_3 as a working electrode and the CNTf-SiO_2 as a counter electrode. During operation, the brackish water was fed from the bottom of the CDI reactor and was collected, once processed, at the top of the opposite end. The flow circuit consists of a vessel filled with the electrolyte solution, the CDI cell and a calibrated Masterflex Model 77521-47 pump fitted with a Masterflex pump head Type 7518-00, interconnected with Viton® tubing. The tubing was connected to the cell entries and exits with PTFE connectors. All experiments were performed by using Ar pumping in the electrolyte container.

Fabrication of MOx-CNTf electrodes. Recent studies indicated that by constructing long CNTs as fibers their tensile properties as well as electrical conductivity or specific surface area could be greatly enhanced.[35] The use of carbon nanotube fibers (CNTf) as electrodes in electrochemical devices depends, in general, on their textural properties, capacitance and electronic structure and on the orientation and size of the network as well. Textural characteristics such as porosity are directly linked to inter and intraparticle properties. Pores represent areas with imperfect packing that are exposed to foreign molecules. Whereas, most stress and charge transfer domains are located in contact points which are regions of well-stacked CNTs in bundles or other fiber subunits. CNTf can be synthesized by different procedures:[35] i) Direct spinning from the gas-phase during CNT synthesis by chemical vapor deposition. ii) Drawing from a forest of vertical CNTs. iii) Wet-spinning of nanocarbons dispersed in liquid (lyotropic liquid crystalline dispersions or polymer-CNT dispersions). In this study, direct spinning from the gas-phase during CNT synthesis by CVD was used to fabricate CNTf-based composites as can be seen in **Figure S2**.

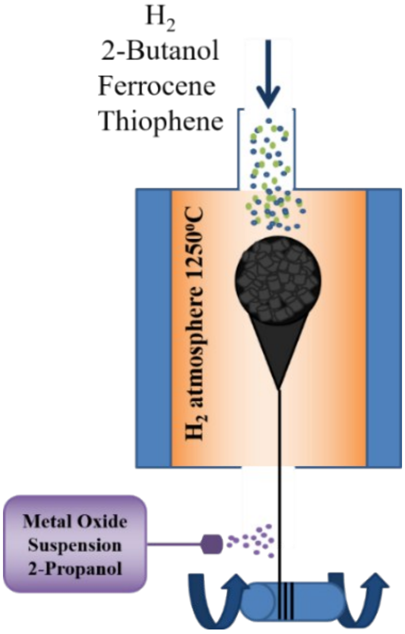

Figure S2. Scheme of direct spinning from the gas-phase during CNTf synthesis by CVD. Source: modified from.[35]

Electrophoretic mobility curves as a function of pH of MOx sol particles in aqueous solutions of $NaNO_3$. To obtain zeta potential values of samples dispersions (nanoparticles of silica and bohemite, γ-Al_2O_3 precursor) a ZetaSizer (Malvern Instrument, Nano series) was employed equilibrated at various pH values: it was coupled with an Autotitrator that used 0.05 M NaOH and 0.05 M HNO_3 solutions to adjust the pH of these suspensions. As shown in **Figure S3**, the two metal oxide suspensions exhibit, over a wide range of pH, zeta potentials of opposite sign: silica exhibits a negative surface potential (at pH > 3) and bohemite (γ-Al_2O_3 precursor) a positive zeta potential (at pH < 10). Interestingly, the potential difference of the particles is a maximum within a pH range from 6 and 8, which it is the pH range of drinkable water. Thus, the development of a surface potential depending on pH conditions may have a great impact on electrosorption-based processes such as capacitive deionization, not only during the ion's adsorption but also the surface potential prevents ions to be re-adsorbed onto the electrodes' surfaces during the regeneration stage.

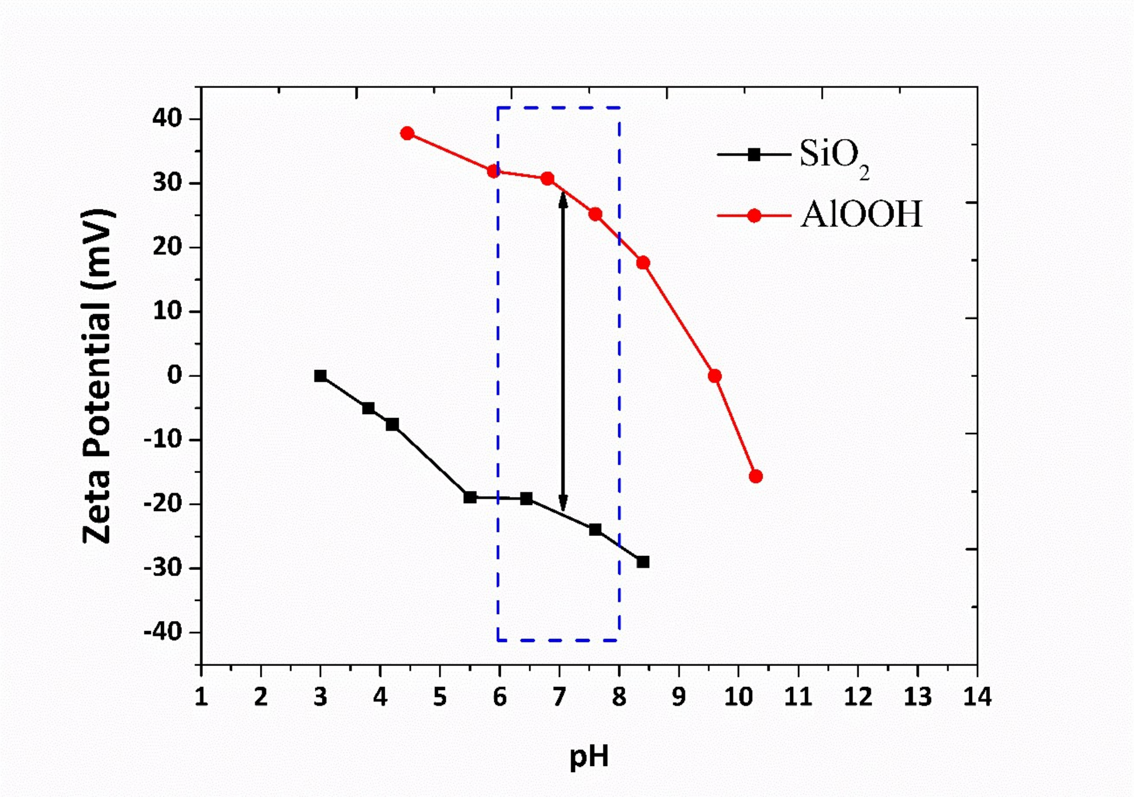

Figure S3. Zeta potential as a function of pH for γ-AlOOH and SiO_2 particles in aqueous solution.

Images of electron micrographs of MOx/CNTf at different magnifications.- Metal oxide particles are dispersed not only on the top layer of the fibers, but also into the structure filing the voids or pores of the fibers. To confirm this statement, SEM images obtained by using back-scattered electrons (BSE) detector were also included to determine the number of phases as well as their dispersion in these samples. In the SEM-Images of γAl_2O_3-CNTf composites (**Figure S4**(a.1-c.1)) the presence of γ-Al_2O_3 can be discerned. Accordingly, by implementing a BSE detector, the incorporation and distribution of γ-Al_2O_3 nanoparticles can be well distinguished. The presence of a higher atomic number phase in CNTfs can be clearly observed by comparing upper and down files; the brighter areas correspond to the metal oxide phase. Furthermore, BSE images corroborate the increment of γ-Al_2O_3 content of the different samples and the homogeneity of the spraying process. Moreover, in Figure S4(a.1) and (b.1), in (c.1), γ-Al_2O_3 does appear to be forming a layer of a few nm thick around the carbon fibers found in the CNTf (see inset magnified view). In this case, metal oxide layers of 100 to 500 nm thick were observed.

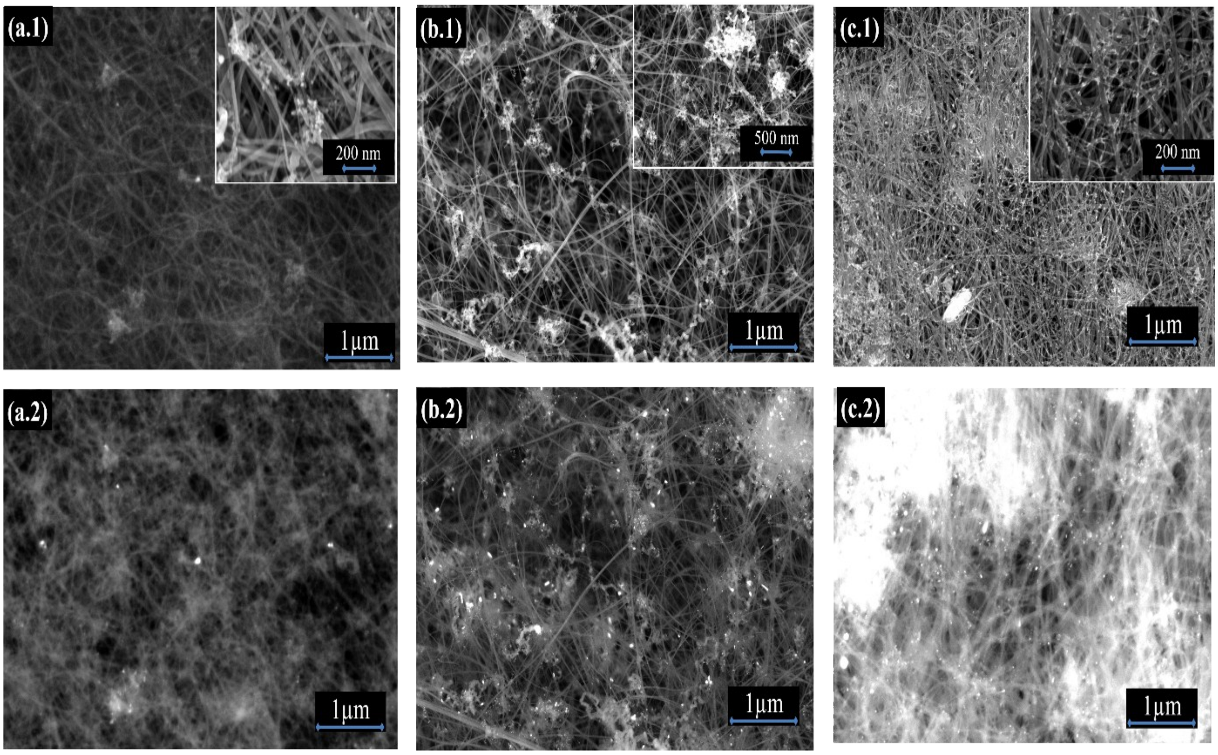

Figure S4. SEM Images of γAl_2O_3-CNTf Composites. **a)** 6 wt.% γAl_2O_3-CNTf. **b)** 21 wt.% γAl_2O_3-CNTf; **c)** 43 wt.% γAl_2O_3-CNTf. Number 1 corresponds to SEM images, 2 to SEM-BSE images.

In the case of SiO_2-CNTf SEM images, some considerations reported in previous studies were taken into account.[47,44] In these studies, a gel formation was observed due to the fact that the SiO_2 sol during the coating of the electrodes was near to its isoelectrical pH. In order to evaluate the structure of carbon nanotubes fibers with SiO_2 nanoparticles under the possibility of a gelling process, SEM images are summarized in **Figure S5.**

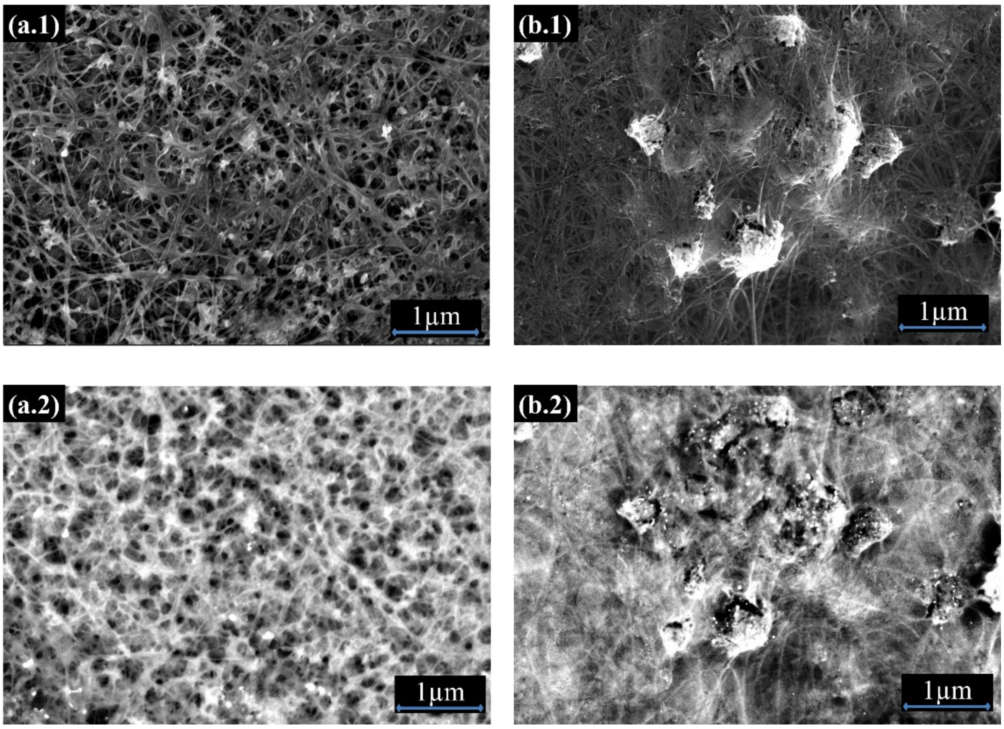

Figure S5. SEM Images of SiO_2-CNTf Composites. **a)** 21 wt.% SiO_2-CNTf. **b)** 60 wt.% SiO_2-CNTf. Number 1 corresponds to SEM images, 2 to SEM-BSE images.

The presence of SiO_2 nanoparticles is confirmed by these images. SiO_2 suspension not only covered the CNTf but also, appeared to gel. Despite gelling process, a 21 wt.% concentration does not disrupt the carbon nanotube fibers network (Figure S5a). However, when SiO_2 content is increased (Figure S5b) large membrane/plate like structures between filaments appear and cover the CNTf surface. SiO_2 gel formation provoked a negative effect in electrical conductivity of the composite: pristine fibers reduce its conductivity from 160 S cm^{-1} to 88 S cm^{-1} when the contain of SiO_2 attained 60 wt.%. On the contrary, the sample prepared with 21 wt.% SiO_2 content in which the gelling process was not so extended showed only a slight increase of its resistivity (157 S cm^{-1}).

TG Analysis. To determine the γ-Al_2O_3 and SiO_2 content in composites, TG Analysis was performed for different samples including CNTf without any metal oxide incorporation. In **Figure S6**a and Figure S6b the percentage of mass remaining of the different samples is plotted at different temperatures. As can be seen in these graphs, there is a 5 wt.% remained in carbon nanotube pristine sample (CNTf). This percentage corresponds to the residual iron oxide content due to the use of ferrocene as catalyst during the CNTf synthesis.[34] Therefore, that value is taken into account in composite samples and it is being subtracted to calculate the wt.% of γ-Al_2O_3 and SiO_2 that has been incorporated into the fibers network. Thus, percentage values shown in legends of Figure S6 correspond to the final amount of γ-Al_2O_3 or SiO_2.

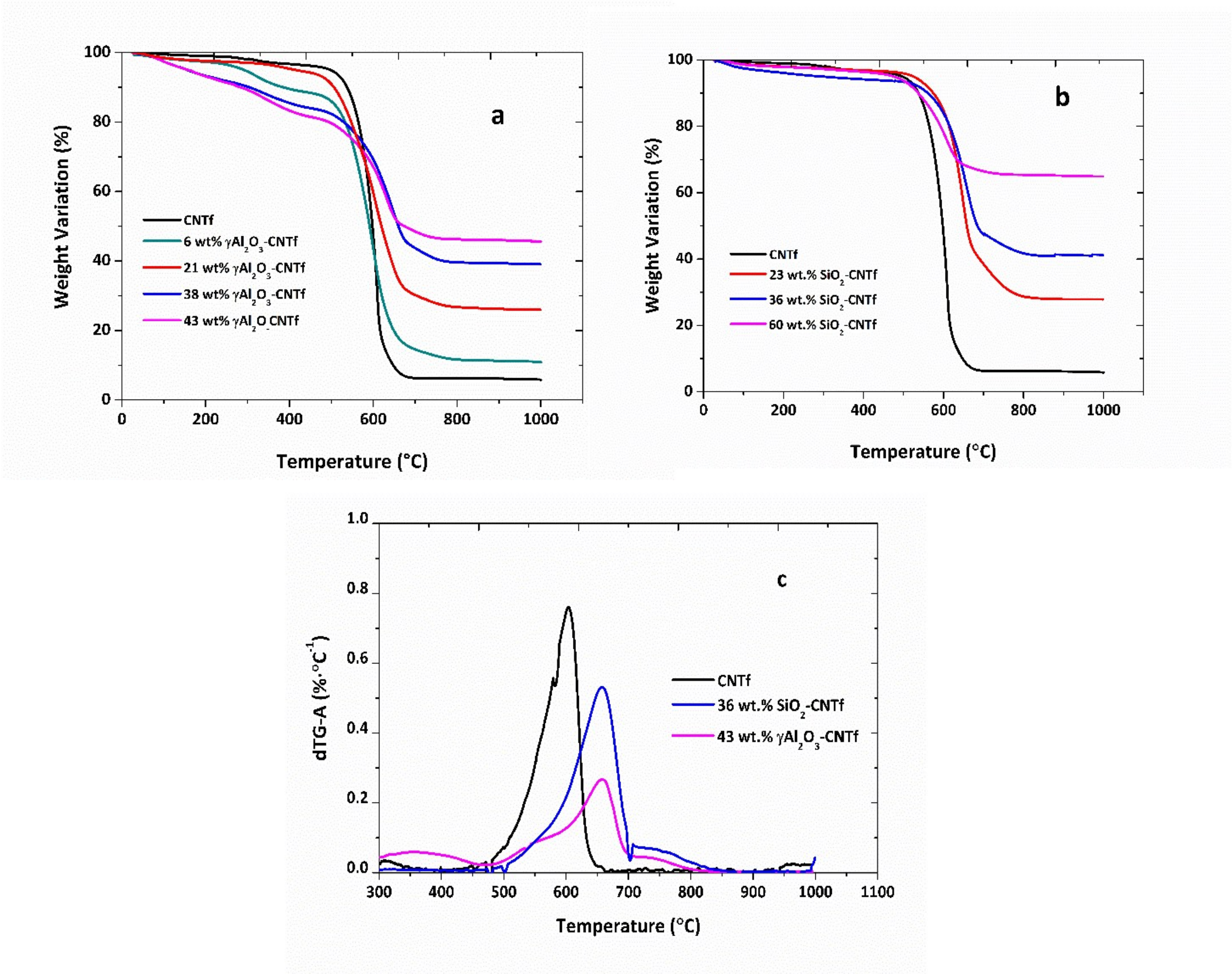

Figure. S6. a) TG-curves of different γAl_2O_3-CNTf Composites. **b)** TG-curves of different SiO_2-CNTf Composites. **c)** DTGA: CNTf, 36 wt.% SiO_2-CNTf and 43 wt.% γAl_2O_3-CNTf.

Regarding the electrodes made of carbon nanotube fibers coated with alumina γ-Al_2O_3, in Figure S6a, there are two types of samples. Samples of 6 wt.%, 38 wt.% and 43 wt.% were directly analyzed by TGA before firing step whereas 21 wt.% γ-Al_2O_3 corresponds to a sample previously heated up in air at 350 ^{0}C for 2.5 h prior to TG-Analysis. The aim of this modification was to confirm the transformation of γ-AlOOH into γ-Al_2O_3 at 350 ^{0}C producing water vapor in the process: 2 γ-AlOOH$\rightarrow$ γ-Al_2O_3+ H_2O .[47] Thus, in its TG-curve no weight loss is observed at 350^{0}C as bohemite was previously transformed during the firing process. Accordingly, there is a loss in weight at 350°C for the three samples that were not previously fired which is directly linked to this gas-phase oxidation process.

In Figure S6b, it is also subtracted the residual iron content of the CNTf to calculate the SiO_2 content of the composites. However, distinctly to carbon nanotube fibers coated with alumina, SiO_2 did not suffer any modification based on a structural oxidation. In this case, none of the samples was previously heated at 350 °C. Moreover, it should be mentioned from Figure S6.C that when the percentage of metal oxide increases, higher temperature stability was achieved. This result is related to the higher thermal stability of metal oxides which are normally used to protect surfaces from thermal degradations. Thus, Figure S6c shows that for both metal oxides, the degradation temperature of the composite is increased from 600 °C to 650 °C when the oxides were incorporated to the carbon nanotube fibers pore structure reaching more thermal stability.

Cyclic Voltammetry measurements. CV experiments were preformed to examine the electrochemical properties of the hybrid electrodes in comparison with the pristine CNTf

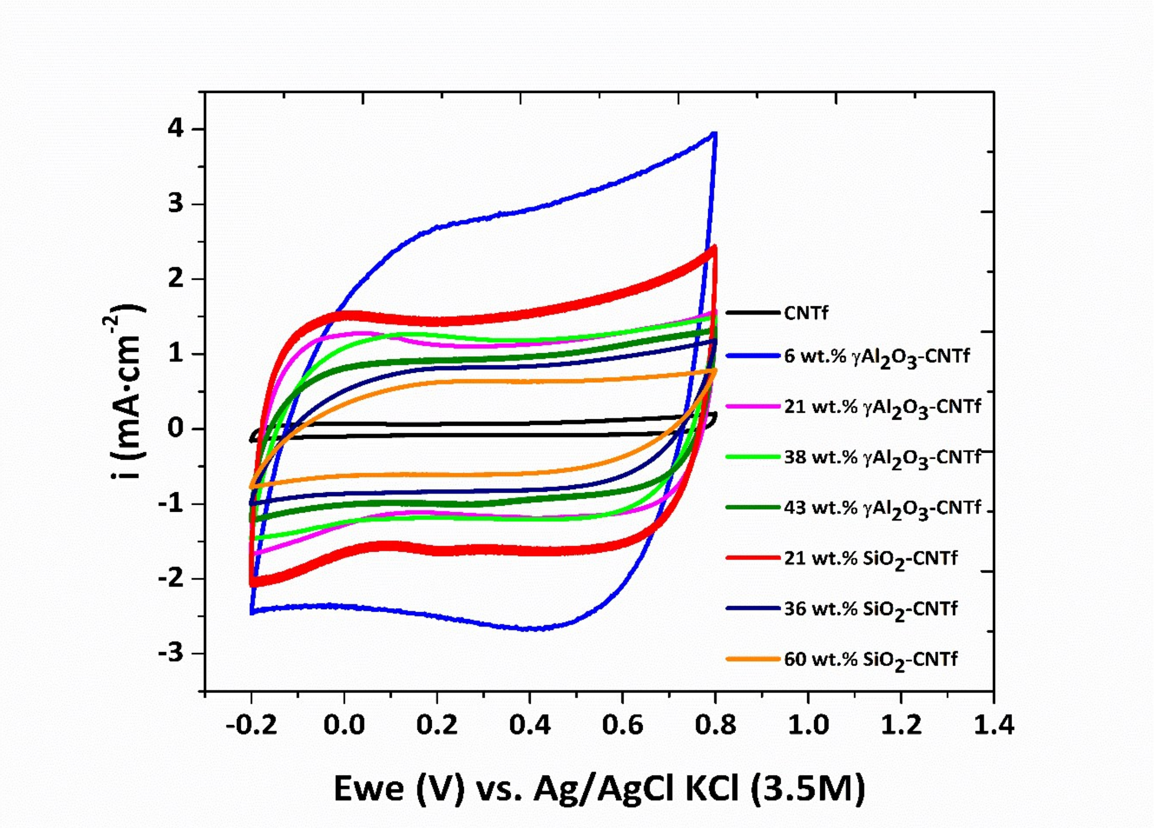

Figure S7. Cyclic Voltammetry curves for all MOx-CNTf based composites in neutral aqueous media and 100 mV s^{-1}.

All MOx/CNTf composites electrodes show not only significantly higher areas under the CV curves than pristine CNTf electrodes, but also a supercapacitor shape-like. These results reveal that a porous metal oxide network interpenetrated into porous fibres of carbon nanotubes results in a large increase in the electrochemical capacitance of CNTf based electrodes. This is mainly associated to the singular electrical double-layer formed by these metal oxides due to their intrinsic surface potential as well as their well-known wettability properties. Moreover, for both SiO_2 and γ-Al_2O_3 based composites, it can be observed that a significant increase in the metal oxide content also lead to a reduction in the area under the curve. These effect might be linked to a reduction in electrical conductivity associated to the insulating nature of these metal oxides.

Swagelok cell configuration. "T-Type" configuration (**Figure S8**a) for cyclic voltammetry tests and two-electrode connection cell (**Figure S8**b) in galvanostatic charge-discharge as well as in spectroscopy techniques, respectively.

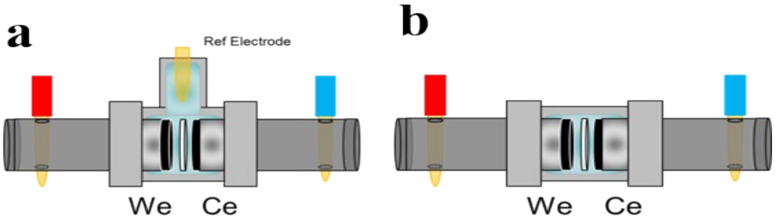

Figure S8. Swagelok® Cell schemes: **a)** Three-Electrode Connection: T-Type, **b)** Two-Electrode Connection.

Estimation of the MOx content (wt.%) to electrode spontaneous wetting/wicking. Wetting of CNTf-based electrodes is the displacement of an electrode-air interface with an electrode-liquid interface. However, Young's equation should not be used to estimate wettability of MOx/CNTf electrodes as they are porous materials and they develop a spontaneous flow due to capillary forces (wicking). For a spontaneous wetting/wicking, the associated free energy change must be a negative value <ΔG. Accordingly, the change of Gibbs free energy (ΔG) for the wetting/wicking, at room temperature, as a function of MOx wt.% is estimated to determine the critical mass fraction of MOx required for spontaneous electrolyte infiltration. As explained in details in a previous work done by Multifunctional Nanocomposites Group, [6] **Equation S1** it is used to calculate Gibbs free energy:

$$\Delta G = A_{BET}(\gamma_{SL} - \gamma_{SV}) \qquad \text{(S1)}$$

Where A_{BET} is the BET surface area, equivalent to the free internal area, γ_{SL} and γ_{SV} are surface energy at the solid/liquid interface and solid surface energy, respectively. Accordingly, $\gamma_{SL} - \gamma_{SV} < 0$ can be considered the spontaneous wetting/wicking condition. Considering Owens & Wendt study, [7] where γ_{SL} is estimated by the dispersive, γ^d, and polar, γ^p, components of the surface energy. Then, γ_{SL} is calculated by **Equation S2**:

$$\gamma_{SL} = \gamma_{SV} + \gamma_{LV} - 2\cdot\sqrt{\gamma_{SV}^{d}\cdot\gamma_{LV}^{d}} - 2\cdot\sqrt{\gamma_{SV}^{p}\cdot\gamma_{LV}^{p}} \qquad \text{(S2)}$$

Where γ_{LV} is the liquid surface energy. Thus, wetting/wicking condition can be expressed as $\gamma_{LV} - 2\cdot\sqrt{\gamma_{SV}^{d}\cdot\gamma_{LV}^{d}} - 2\cdot\sqrt{\gamma_{SV}^{p}\cdot\gamma_{LV}^{p}} < 0$. γ_{LV} is the sum of its dispersion and polar components, $\gamma_{LV} =$

$\gamma^d_l + \gamma^p_l$. Accordingly, substituting γ_{SL}, γ_{LV} in Equation 2 and considering a MOx/CNTf-based electrode as the solid surface, lead to **Equation S3**:

$$\frac{\Delta G}{A_{BET}} = \left(\gamma_w^d + \gamma_w^p\right) - 2\cdot\left(1 - x_{MOx}\right)\cdot\left(\sqrt{\gamma_{CNTf}^d\cdot\gamma_w^d} + \sqrt{\gamma_{CNTf}^p\cdot\gamma_w^p}\right) - 2\cdot\left(x_{MOx}\right)\left(\sqrt{\gamma_{MOx}^d\cdot\gamma_w^d} + \sqrt{\gamma_{MOx}^p\cdot\gamma_w^p}\right) \tag{S3}$$

Where subscript *w* refers to water and χ_{MOx} is the MOx mass fraction. Using Equation 4, the minimum MOx content into the CNTf network required for the aqueous electrolyte to infiltrate spontaneously the electrode can be estimated. **Table S1** summarizes the surface free energy components of different materials as well as the minimum metal oxide content needed in a Glass/CNTf-based electrodes to show negative Gibbs free energy values when aqueous solution infiltrates them. In a MOx/CNTf-based electrode the estimated critical mass fraction of MOx is around an 8 wt.%. Therefore, in this study it is expected that no electrolyte limitation could affect desalination performance of MOx/CNTf electrodes.

Table S1. Dispersion, polar component of surface free energy, MOx wt.% and change Gibbs free energy for the selected materials.

Materials	Surface Free Energy [mJ m^{-2}]		MOx Content [wt.%]	Gibbs Energy Change [mJ m^{-2}]
	Dispersion, γ^d_i	Polar, γ^p_i		
Water[8]	16	85.5	-	86
CNTf[6]	17.6	10.2	-	9.07
Glass[9],a	32	80	100	-109.15
Glass/CNTf			>7.67	<0

[a)] Due to the lack of literature references of metal oxides surface energy dispersion and polar components, glass is being considered as a representative material to estimate the critical mass fraction of metal oxides for spontaneous wetting/wicking.

Cyclability tests & Raman spectroscopy. Cycling stability of the electrodes is provided in **Figure S9** where capacitance retention ratio is plotted versus cycle number for γAl_2O_3-CNTf and SiO_2/CNTf electrodes. Moreover, it is included the cyclic stability for an asymmetric cell based on γAl_2O_3-CNTf and SiO_2/CNTf as anode and cathode, respectively. It is confirmed the appropriate cycle performance of these electrodes for CDI devices (**Figure S9**a). It can be observed the lack of capacity fading with cycles, confirming the appropriate cycle performance of these electrodes for CDI applications. Additionally, Raman spectroscopy profiles corroborate the unaltered properties of the electrodes after cycling in the CDI flow-cell (**Figure S9**b).

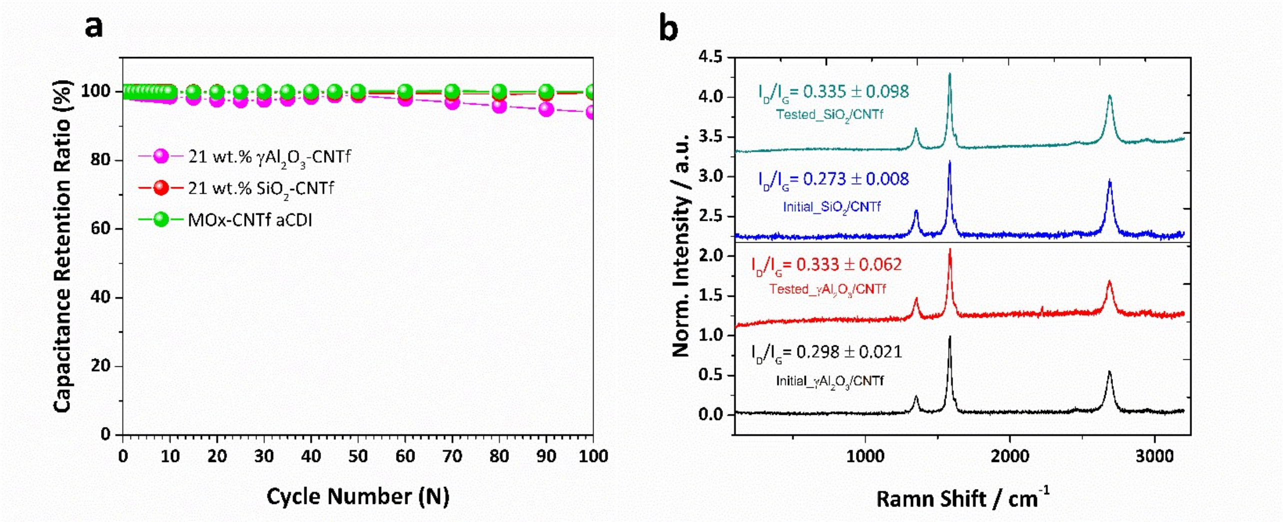

Figure S9. a) Capacitance retention ratio (%) versus cycle number (N) of 21 wt.% γAl$_2$O$_3$-CNTf, 21 wt.% SiO$_2$-CNTf electrodes in symmetric Swagelok® Cell configuration and an asymmetric cell (21 wt.% % γAl$_2$O$_3$-CNTf, 21 wt.% % SiO$_2$-CNTf electrodes) assembled in Swagelok® Cell two-electrode connection.

Electronic Supplementary Information References

1 J. J. Vilatela and R. Marcilla, *Chem. Mater.,* 2015, **27**, 6901–6917.

2 J. J. Lado, J. J. Wouters, M. I. Tejedor-Tejedor, M. A. Anderson and E. Garcia-Calvo, *J. Electrochem. Soc.*, 2013, **160**, E71–E78.

3 J. J. Wouters, M. I. Tejedor-Tejedor, J. J. Lado, R. Perez-Roa and M. A. Anderson, *J. Electrochem. Soc.,* 2016, **163**, A2733–A2744.

4 E. Senokos, V. Reguero, J. Palma, J. Vilatela and R. Marcilla, *Nanoscale*, 2016, **8**, 3620–3628.

5 K. C. Leonard, J. R. Genthe, J. L. Sanfilippo, W. A. Zeltner and M. A. Anderson, *Electrochim. Acta*, 2009, **54**, 5286–5291.

6 Hangbo Yue, *Polymer interaction with macroscopic carbon nanotube fibres and fabrication of nanostructured composites*, Universidad Politécnica de Madrid, July, 2015.

7 D. K. Owens and R. C. Wendt, *Journal of Applied Polymer Science*, 1969, 13, 1741-1747.

8 J. Qiu, J. Terrones, J.J. Vilatela, M.E. Vickers, J.A. Elliot and A. H. Windle. *ACS Nano* 2013, **7**, 8412-8422.

9 E. Chibowski, L. Hołysz, G. A. M. Kip, A. van Silfhout, H. J. Busscher, *Journal of Colloid and Interface Science*, 1989, **132**, 54-61.